https://doi.org/10.1016/j.jbiomech.2020.109841

Title:

Modeling of braided stents: Comparison of geometry reconstruction and contact strategies

Authors:

Alissa Zaccaria[1], Francesco Migliavacca[1], Giancarlo Pennati[1], Lorenza Petrini[2]

[1] LaBS, Dept. of Chemistry, Materials and Chemical Engineering, Politecnico di Milano, Milan, Italy

[2] Dept. of Civil and Environmental Engineering, Politecnico di Milano, Milan, Italy

Corresponding author:

Prof. Lorenza Petrini, PhD

Department of Civil and Environmental Engineering

Politecnico di Milano

Piazza Leonardo da Vinci, 32

20133 Milano (Italy)

tel: +39.02.2399.4307

fax: +39.02.2399.4286

E-mail: lorenza.petrini@polimi.it

Keywords:

Self-expandable stent

Nitinol

Finite element analysis

3D parametric equations

wire interaction

Word counts: ('Introduction' through 'Discussion and conclusion') 3484

Abstract (words: 244)

Braided stents are self-expandable devices widely used in many different clinical applications. In-silico methods could be a useful tool to improve the design stage and preoperative planning; however, numerical modeling of braided structures is not trivial. The geometries are often challenging, and a parametric representation is not always easily achieved. Moreover, in the literature, different options have been proposed to handle the contact among the wires, but an extensive comparison of these modeling techniques is missing. In this work, both the geometry and contact issues are discussed. Firstly, an effective strategy based on parametric equations to draw complex braided geometries is illustrated and exploited to build three beam meshes resembling commercial devices. Secondly, three finite element simulations (bending, crimping and confined release) were carried out to compare simplified contact techniques involving connector elements with the more realistic but computationally expensive option based on the general contact algorithm, which has already been validated in the literature through comparisons with experimental results. Both local (stress distribution) and global quantities (forces/displacements) were analyzed. The results obtained using the connectors are significantly affected by wire interpenetrations and over-constraint. The percentage errors reached considerably high values, exceeding 100% in the confined release test and 50% in the remaining cases study. Moreover, the errors do not show uniform trends but vary according to the stent geometry, boundary conditions, connector type and investigated entity, suggesting that it is not possible to replace the use of the general contact algorithm with simplified approaches.

Introduction

The introduction of stents significantly influenced vascular surgery by establishing a valuable alternative to traditional surgery techniques. Despite the good results obtained so far, some problems remain (McHugh et al., 2016). In-silico models can be a powerful tool to investigate the behavior of endoprosthesis improving the design and optimization stages, and supporting the pre-operative planning (Karanasiou et al., 2017; Morlacchi and Migliavacca, 2013). Numerical methods have been extensively used in the literature to analyze the biomechanical behavior of stents. From a structural point of view, the crimping and expansion process assessment (Debusschere et al., 2015), the post-implantation evaluation and the structural or functional problems concerning the device or the native vessel (Auricchio et al., 2011; Derycke et al., 2019; Sturla et al., 2016), the long-term event like degradation (Gastaldi et al., 2011) and fatigue fracture (Azaouzi et al., 2013; Petrini et al., 2016) have been investigated. Fluid dynamic studies were also carried out to investigate the blood flow alterations (Cebral et al., 2011), the wall shear stresses (Chiastra et al., 2016; Gundert et al., 2012; Midulla et al., 2012) or the drug distribution in case of drug eluting stents (Balakrishnan et al., 2005).

Braided stents belong to the multitude of commercial devices available nowadays for endovascular treatment (Bishu and Armstrong, 2015; Ronchey et al., 2016). They are self-expandable consisting of interlaced wires, which provide great flexibility and kinking resistance. Both metallic and polymeric materials are adopted for their manufacturing. They are proposed for several applications (Han et al., 2006; Irani and Kozarek, 2010; Isotalo et al., 2006; Raju, 2013), including the treatment of stenotic peripheral arteries (Cremonesi et al., 2015), intracranial aneurysms (Briganti et al., 2015) and for the aortic valve replacement (Seigerman et al., 2019).

Analytical models, considering not-interacting helical wires, were proposed to predict the behavior of braided stents subjected to idealized boundary conditions (Jedwab and Clerc, 1993; Wang and Ravi-Chandar, 2004a, 2004b; Záhora et al., 2007). Numerical methods, particularly finite element methods (FEM), allow to analyze also more complex situations involving intricate geometries, nonlinearities, interactions, and dynamic conditions. However, the numerical studies available are few, if compared to those related to laser-cut devices, and they are described below.

The main issues related to their numerical modeling are: the geometry reconstruction and the description of the high number of contacts among the wires.

For what concerns the geometry reconstruction, two solutions were proposed in the literature. Some research groups adopted the open-source software PyFormex developed at Ghent University (Verhegghe, 2013) which, following a sequence of mathematical transformations, generates the mesh of the stent (Conti, 2007; De Beule et al., 2009; Peirlinck et al., 2018; Shanahan et al., 2017a, 2017b). On the other hand, Kim et al. (Kim et al., 2008) and, more recently, Zhao et al. (Zhao et al., 2019) presented an analytical formula to build cylindrical open ends devices. However, a similar strategy has not yet been applied for more complex geometries.

Given the significantly lower computational cost respect to three-dimensional (3D) elements, beam elements are usually chosen to model the wires (Auricchio et al., 2011; Conti, 2007; De Beule et al., 2009; Kim et al., 2008; Ma et al., 2012; Peirlinck et al., 2018; Shanahan et al., 2017a, 2017b; Záhora et al., 2007; Zhao et al., 2012). Beam meshes offer different options to describe the interaction within the stent elements. The most realistic one consists of representing all the contacts and relative slips among the wires (Kim et al., 2008; Ma et al., 2012; Zhao et al., 2012). However, this approach is computationally demanding. Accordingly, in the literature, simplified methods were proposed, where the relative motions of two interacting wires are restricted, introducing connector elements in the contact points where the wires are crossing. In particular, the connectors usually adopted are the join (Auricchio et al., 2011; Conti, 2007; De Beule et al., 2009) and the hinge (Shanahan et al., 2017b, 2017a). In particular, the connectors usually adopted are the join (Auricchio et al., 2011; Conti, 2007; De Beule et al., 2009) and the hinge (Shanahan et al., 2017b, 2017a). The first option joins the relative position of two nodes (no relative displacements between the contact points), while a revolute constraint is added in the latter case, permitting only relative rotations around the local radial direction of the intersecting cross-sections. Notwithstanding the computational advantage, to the best of our knowledge, an extensive comparison between these two approaches and the most realistic one, to verify their level of accuracy, is lacking.

In this context, the present work aims to go further the literature results, both for what concerns the geometry reconstruction and for the identification of the most suitable contact model. Accordingly, the paper has two main objectives.

The first one is to propose an effective strategy to build complex braided geometries: the analytical approach is preferred due to the versatility of a mathematical description. The 3D parametric equations that allow replicating devices characterized by open or looped ends and cylindrical or variable section geometries (Fig. 1) are illustrated.

The second goal is to give indications about the opportunity of using simplified contact methods. A deep comparison is performed among the finite element strategies described above to model wire contacts: three different braided stents are considered and their performance under different working conditions (bending, crimping, and confined release) are compared, taking into account global (reaction force/moment, displacement) and local quantities (stress/strain).

Materials and methods

A code was developed using MATLAB (MathWorks, Natick, MA, USA) to build three stent models resembling three commercial devices for peripheral artery stenting with different structural features: Wallstent (Boston Scientific, Marlborough, MA, USA), Supera (Abbott Vascular, Santa Clara, CA, USA), and Roadsaver (Terumo, Tokyo, Japan). The code returns to the user the nodes, elements, and connectors lists (pair of nodes whose relative motions are constrained by connector elements). Subsequently, the models were imported in the finite element code Abaqus 2018 (Dassault Systemes Simulia, Providence, RI, USA), where the material parameters, connector sections (hinge/join) or interaction property, and boundary conditions were defined.

Stents reconstruction

The wires were drawn using 3D parametric equations in which a sinusoidal component describes the intertwining. The meshes were obtained by sampling the ϑ parameter (Fig. 1).

The Wallstent is a cylindrical open ends braided stent. The repetitive unit of the counter-clockwise wire follows the set of equations (1), wherein R, r, n, α, L correspond respectively to the stent middle radius, the wire radius, the number of the clockwise wires, the pitch angle and the stent length (Fig. 1).

$$\begin{cases} x(\vartheta) = (R + r \cdot \cos(\vartheta \cdot n)) \cdot \cos(\vartheta) \\ y(\vartheta) = (R + r \cdot \cos(\vartheta \cdot n)) \cdot \sin(\vartheta) \\ z(\vartheta) = R \cdot \vartheta \cdot \tan(\alpha) \end{cases}$$

$$with\ \vartheta \in \left[0, \frac{2\pi}{n}\right] \qquad (1)$$

The Supera stent, in contrast to the previous one, is a looped ends device. The central trait follows the same equations of the Wallstent model while the extreme portions need to be modified to join the clockwise wires with the counter-clockwise ones. Specifically, the oscillation amplitude was halved, and a quadratic term of the form $a \cdot (\vartheta - \vartheta_0)^2$ was subtracted on the longitudinal coordinate for $\vartheta \in$

$\left[\vartheta_0, \frac{\pi}{n}\right]$. The parameter $'\vartheta_0'$, which determines the sharpness of the terminal loops, was set equal to 0. Thus, the parameter $'a'$ was obtained by imposing the tangency on the extremities ($z'(\vartheta = \pi/n) = 0$).

$$\begin{cases} x(\vartheta) = \left(R + \frac{r}{2} \cdot (1 + \cos(\vartheta \cdot n))\right) \cdot \cos(\vartheta) \\ y(\vartheta) = \left(R + \frac{r}{2} \cdot (1 + \cos(\vartheta \cdot n))\right) \cdot \sin(\vartheta) \\ z(\vartheta) = (\vartheta - \vartheta^2 \cdot n/(2\pi)) \cdot R \cdot \tan(\alpha) \end{cases}$$

$$with\ \vartheta \in \left[0, \frac{\pi}{n}\right] \tag{2}$$

The external mesh of the Roadsaver stent is characterized by a variable section diameter. To represent the conical shape of the terminal traits, the radius and the length were expressed as linear functions of ϑ and the oscillation term was split between the radial and the longitudinal coordinate.

$$\begin{cases} x(\vartheta) = \left(R + \Delta R \frac{\vartheta}{2\pi/n} + r \cdot \cos(\vartheta \cdot n) \cdot \cos\left(\operatorname{atan}\left(\frac{\Delta R}{\Delta Z}\right)\right)\right) \cdot \cos(\vartheta) \\ y(\vartheta) = \left(R + \Delta R \frac{\vartheta}{2\pi/n} + r \cdot \cos(\vartheta \cdot n) \cdot \cos\left(\operatorname{atan}\left(\frac{\Delta R}{\Delta Z}\right)\right)\right) \cdot \sin(\vartheta) \\ z(\vartheta) = \Delta Z \cdot \frac{\vartheta}{2\pi/n} - r \cdot \cos(\vartheta \cdot n) \cdot \sin\left(\operatorname{atan}\left(\frac{\Delta R}{\Delta Z}\right)\right) \end{cases}$$

$$with\ \vartheta \in \left[0, \frac{2\pi}{n}\right] \tag{3}$$

Where ΔR and ΔZ are the radius and length variation respectively related to the interval of the parameter ϑ considered ($2\pi/n$). Note that the illustrated equations may be extended to describe even more complex geometry. The general form is:

$$\begin{cases} x(\vartheta) = \left(R + \Delta R(\vartheta) + r \cdot \cos(\vartheta \cdot n) \cdot \cos\left(\operatorname{atan}\left(\frac{dR}{dz}(\vartheta)\right)\right)\right) \cdot \cos(\vartheta) \\ y(\vartheta) = \left(R + \Delta R(\vartheta) + r \cdot \cos(\vartheta \cdot n) \cdot \cos\left(\operatorname{atan}\left(\frac{dR}{dz}(\vartheta)\right)\right)\right) \cdot \sin(\vartheta) \\ z(\vartheta) = \Delta Z(\vartheta) - r \cdot \cos(\vartheta \cdot n) \cdot \sin\left(\operatorname{atan}\left(\frac{dR}{dz}(\vartheta)\right)\right) \end{cases}$$

$$with\, \vartheta \in \left[0, \frac{2\pi}{n}\right] \qquad (4)$$

Table 1 (top) reports the geometrical parameters of each model where *Rext=R+2r* and the number of beam elements (B31) chosen after a mesh sensitivity analysis (see Appendix A). Fig. 1 shows the final reconstructed geometries.

Material and contact definition

The Wallstent is made of Phynox, a cobalt-chromium alloy; the Supera and Roadsaver devices are made of Nitinol, a nickel-titanium alloy featuring super-elastic behavior above a specific temperature value (Af). Details about the mechanical models and material parameters used are reported in the Appendix B.

To describe the contact among the wires, three different strategies were analyzed: i) general contact (GC) algorithm (hard contact in the normal direction and friction coefficient equal to 0.2 in the tangential direction (Ma et al., 2012)), ii) hinge connectors (H) and iii) join connectors (J) (the stent cylindrical coordinate system was used to define univocally the radial direction (Fig. 1)). The correctness of the simplified models involving connector elements was evaluated considering the GC strategy as the reference standard, given the greater accuracy of the contact description. For the H and J strategies both the implicit and the explicit solvers can be used, while the GC model needs to be solved in explicit due to the high nonlinearity introduced by the extremely large number of contacts within the stent components. The simulations herein presented were conducted using the explicit solver, once verified that, as regards connector models, quasi-static explicit simulations were comparable with solutions provided by the implicit solver.

The GC model was previously validated replicating one of the localized compression tests performed by Kim et al. (Kim et al., 2008) who provided both experimental and numerical curves. The details and results of the validation process are reported in Appendix B.

Simulations

For each stent model three simulations were carried out (bending, crimping and confined release) using the two types of connectors or general contact algorithm, for a total of 27 computational analyses. For the Supera and Roadsaver stents, the temperature was set constant and equal to 22°C (>Af) in all the simulations. Since the aim of the study is purely comparative, the specific temperature value chosen for the analyses does not affect the findings. Smooth step amplitudes, appropriate mass-scaling factor and linear bulk viscosity were set to optimize the computational time and to avoid instability. In all the simulations, the kinetic energy and the viscous dissipations were kept lower than the 5% compared to the internal energy throughout most of the process.

Bending

Two reference points (RP1 and RP2 in Fig. 2a) were introduced on the stent axis (Z-axis) and were associated with the end nodes through multiple-point constraints (MPC) using beam connections. A rotation of 1.5 radiant around the X-axis was imposed on the defined nodes, and all other degrees of freedom were locked apart for the Z translation of RP2. For each simulation, in addition to the deformed configurations and stress distribution, the following quantities were evaluated: reaction moment in RP1, Z-displacement of RP2 and Y-displacement of the middle section.

Crimping

For the crimping simulation, 12 rigid surfaces were introduced and radially moved to reduce the diameter of each stent to 1.85mm (Fig. 2b). To stabilize the model, the longitudinal displacements of two symmetrical points in the middle section of the stent were prevented. A frictionless interaction was defined between the stent and the rigid planes. The comparison between the different strategies for simulating the interaction within the stent elements was performed in terms of deformed configuration, stress distributions and significant quantities, namely: crimping force, length variation and diameter variation (evaluated both in the middle and side sections).

Confined expansion

Finally, the stent release in an idealized rigid stenotic vessel with a concentric plaque was simulated (Fig. 2c). From the crimped configuration, the rigid planes were moved back to their initial position and the interaction between the stent and the vessel internal wall was activated. Hard contact in the normal direction and a penalty factor of 0.2 were chosen (Dordoni et al., 2014). The internal contour of the stenosis was drawn following the Hicks-Henne function (Dordoni et al., 2014):

$$y = \frac{D_V}{2} \times (1 - RS) \times \sin\left(\pi \times \frac{x}{L_p}\right)^s \qquad (1)$$

The values used for the healthy vessel inner diameter (D_v), residual stenosis (RS), plaque length (L_p) and sharpness of the peak (s) are reported in Table 1. The deformed configurations, stress distributions, contact pressure distributions, and forces acting on the confinement surfaces were considered in the comparison.

Results

Table 2 reports the percentage differences of the H and J model with respect to the general contact option, in terms of reaction moments/forces, maximum von Mises stress and displacements/deformations entities.

Bending

Remarkable differences among the stress distribution are visible between the GC and H and J connector models, except when the J model is applied to the Supera geometry. Indeed, the deformed configurations of the Wallstent and Roadsaver significantly vary in accordance with the contact strategy (Fig. 3).

Fig. 4 compares the trend of the reaction moment in the fixed reference point RP1, the Z displacement of RP2 and the Y displacement of the central section, obtained as the mean between the displacements of two symmetrical points.

The H strategy overestimates the final reaction moment of the Wallstent, Supera and Roadsaver models by 14%, 58% and 69% respectively. The differences decrease if the J option is considered, especially for the Supera geometry where the error at the end of the test is lower than the 4%.

The difference on the Z displacement at the end of the test exceeds 15% and 30% for the H and J option respectively except for the Supera stent where the discrepancies are reduced to 1.30% and 5.25%. The maximum deviation of the Y displacement is visible in the Wallstent model, where it reaches the 3.71% for the H option and 6.17% for the J one.

Crimping

The deformed configurations with the Von Mises stress colored maps are reported in Fig. 5. Significant differences are visible on the extremities, where the connector elements are not able to describe relative slips among the wires and to prevent wires overlapping.

The crimping force, the diameter variations (evaluated both in the middle and in the side sections) and the length variation are reported in Fig. 6. To assess the radial stiffness, the sum of the reaction forces acting on the rigid planes was evaluated. The elongation and the diameter variation were determined as the mean of the distance variations between two pairs of opposite nodes.

When applied to the Wallstent geometry, the connector models report a quite similar trend of the reaction force with respect to the GC model throughout most of the process, while greater differences are visible for the looped ends structures.

Differences among the diameter variations in the middle section are visible only for the variable section device, where the GC model predicts an initial increase of this entity before the contact between the planes and the central trait of the stent occurs. Instead, when the side sections are considered, the discrepancies are more evident. Especially for the Wallstent geometry where there is a deviation of 19.44% and 10.45% for the H and J model, respectively. Note that in the open ends device, when the GC strategy is adopted, the side nodes can be subdivided into two subsets (internal and external side nodes highlighted in Fig. 5) whose diameter variation differs by 12.8%. Nevertheless, for clarity, only the mean value is reported in Fig. 6.

The length variations of the three contact strategies are superimposable for the cylindrical geometries, while, if the Roadsaver stent is considered, the connector models present a quite dissimilar trend compared to the GC option, although the final length differs less than 0.5%.

<u>Expansion in an idealized vessel</u>

The deformed configuration of the stent with the associated stress distribution and the contact pressure distribution on the stenotic rigid vessel are reported in Fig. 7. The J model shows similar results compared to the GC strategy for the Supera and Wallstent geometries, even if some variations in the contact pressures distribution are visible. On the other end, the H model overestimates the stress in the central trait for both the cylindrical devices and reports a significantly different configuration for the Wallstent geometry, in which only the central portion of the stent is in contact with the wall. Both the simplified models fail to catch the deformation of the variable section structure.

Fig. 8 shows the comparison among the reaction forces acting on the wall, evaluated both in the middle and in the lateral portions (as a sum of the distal and proximal part) of the vessel. The H model overestimates the force acting on the central trait and underestimates the lateral force, which is null for the Wallstent geometry. The J model shows better results, especially for looped ends geometry. Indeed, the difference on the total force lay below 15%, 7% and 1% for the Wallstent, Supera and Roadsaver, respectively.

Discussion and Conclusions

The building of braided stents is a quite challenging task due to the specific woven structure. Consider the correct distance from the wire centerlines in the overlapping zone and hence the correct local wire curvature is crucial to accurately model this kind of device. Indeed, in certain configurations, the intertwining has consequences from a kinematic as well as a geometric point of view (Appendix D).

In this paper, a simple method for geometry reconstruction, based on the definition of a set of 3D parametric equations, was proposed. The advantage of this approach is that the proposed equations may be easily modified to describe similar braided structures (Irani and Kozarek, 2010), not only stents, by just varying the defined geometrical parameters in a versatile way. Furthermore, it allows for obtaining the analytical description of the stent, the use of which is not limited to finite element analyses.

Three models resembling commercial braided stents were imported in a finite element code and used to compare the response of the different contact modeling techniques to different idealized boundary conditions. The general contact option was considered as the reference standard (Appendix B), and the accuracy of the simplified models, involving connector elements, was assessed. It is possible to notice that both the simplified approaches give different results which underestimate the general contact predictions, but it is difficult to find a general trend. Indeed, the differences are strongly dependent on the geometry and boundary conditions considered.

In general, H and J models are more rigid than the GC one: it means that the connectors prevent movements allowed by friction. However, this trend may be inverted if contacts among the wires, not detected by the connector models, occur when the general contact strategy is applied. This fact explains the final stiffening of the Wallstent and Roadsaver during the crimping simulations (Fig. 6) as well as of the Wallstent during the bending test (Fig. 4), and the underestimation of the final reaction force/moment (Table 2) by the connector models.

In most of the studied cases, the join connector was found to be the best alternative giving the less restrictive constraint, showing smaller differences in terms of deformed shape, stress distributions and reaction forces/moments (Table 2). However, in the case of the bending test on the open ends and variable section devices, the J model allows excessive deformability resulting in significant differences partially smoothed in the H model.

With very few exceptions (such as the J model of the Supera geometry during the bending test (Table 2)), the results of the connector models are strongly influenced by wire interpenetrations and over-constraint. Thus, the general contact option remains the best choice.

One of the advantages of the simplified approach is the possibility to use the implicit solver. Unfortunately, the implicit approach can be exploited only when connectors are employed for running simplistic simulations (such as the tests carried out in this study). Otherwise, also for connectors, it is necessary to carry out explicit quasi-static simulations. Moreover, if all the models (GC, J, and H) are solved with the same setting, the differences in computational time are not relevant.

The limitations of this study include the type of connectors analyzed. In this work, the strategies mainly adopted in the literature were compared. However, more elaborated connector elements could be suggested, for example specifying spring-like behavior, which may be more appropriate than the ones proposed in the literature and analyzed in this study (McGee et al., 2019).

Moreover, only three device geometries were investigated. Also aware of the wide variety of the braided stents, the structures analyzed were assumed adequate to evaluate the impact of three features commonly present in this kind of devices, namely open ends, looped ends and variable sections. Nevertheless, only rotationally symmetrical structures were considered. Therefore, the present strategy does not involve bifurcated or angled stents (Han et al., 2006) that might be included in future developments.

Note that, the present work does not pretend to describe mechanical behavior of the real devices. The simulations are only intended to compare different contact strategies. Thus, the geometries proposed, even if they do not match the commercial stents exactly, are considered meaningful for the stated purpose.

Finally, the proposed modeling strategy involving 3D parametric equations and accurate contact description seems to be a valid tool for deeply investigating the behavior of a large variety of braided stents.

References

Auricchio, F., Conti, M., De Beule, M., De Santis, G., Verhegghe, B., 2011. Carotid artery stenting simulation: From patient-specific images to finite element analysis. Medical Engineering and Physics 33, 281–289. https://doi.org/10.1016/j.medengphy.2010.10.011

Azaouzi, M., Lebaal, N., Makradi, A., Belouettar, S., 2013. Optimization based simulation of self-expanding nitinol stent. Materials and Design 50, 917–928. https://doi.org/10.1007/978-3-642-37143-1_50

Balakrishnan, B., Tzafriri, A.R., Seifert, P., Groothuis, A., Rogers, C., Edelman, B.R., 2005. Strut position, blood flow, and drug deposition: Implications for single and overlapping drug-eluting stents. Circulation 111, 2958–2965. https://doi.org/10.1161/CIRCULATIONAHA.104.512475

Bishu, K., Armstrong, E.J., 2015. Supera self-expanding stents for endovascular treatment of femoropopliteal disease: a review of the clinical evidence. Vascular Health and Risk Management 11, 387–395. https://doi.org/10.2147/VHRM.S70229

Briganti, F., Leone, G., Marseglia, M., Mariniello, G., Caranci, F., Brunetti, A., Maiuri, F., 2015. Endovascular treatment of cerebral aneurysms using flow-diverter devices: A systematic review. Neuroradiology Journal 28, 365–375. https://doi.org/10.1177/1971400915602803

Cebral, J.R., Mut, F., Sforza, D., Löhner, R., Scrivano, E., Lylyk, P., Putman, C., 2011. Clinical application of image-based CFD for cerebral aneurysms. International Journal for Numerical Methods in Biomedical Engineering 27, 977–992. https://doi.org/10.1002/cnm.1373

Chiastra, C., Wu, W., Dickerhoff, B., Aleiou, A., Dubini, G., Otake, H., Migliavacca, F., LaDisa, J.F., 2016. Computational replication of the patient-specific stenting procedure for coronary artery bifurcations: From OCT and CT imaging to structural and hemodynamics analyses. Journal of Biomechanics 49, 2102–2111. https://doi.org/10.1016/j.jbiomech.2015.11.024

Conti, M., 2007. Finite Element Analysis of self-expanding braided wirestent (MSc Thesis, Ghent University).

Cremonesi, A., Castriota, F., Secco, G.G., Macdonald, S., Roffi, M., 2015. Carotid artery stenting: An update. European Heart Journal 36, 13–21. https://doi.org/10.1093/eurheartj/ehu446

De Beule, M., Van Cauter, S., Mortier, P., Van Loo, D., Van Impe, R., Verdonck, P., Verhegghe, B., 2009. Virtual optimization of self-expandable braided wire stents. Medical Engineering and Physics 31, 448–453. https://doi.org/10.1016/j.medengphy.2008.11.008

Debusschere, N., Segers, P., Dubruel, P., Verhegghe, B., De Beule, M., 2015. A finite element strategy to investigate the free expansion behaviour of a biodegradable polymeric stent. Journal of Biomechanics 48, 2012–2018. https://doi.org/10.1016/j.jbiomech.2015.03.024

Derycke, L., Perrin, D., Cochennec, F., Albertini, J.N., Avril, S., 2019. Predictive Numerical Simulations of Double Branch Stent-Graft Deployment in an Aortic Arch Aneurysm. Annals of Biomedical Engineering 47, 1051–1062. https://doi.org/10.1007/s10439-019-02215-2

Dordoni, E., Meoli, A., Wu, W., Dubini, G., Migliavacca, F., Pennati, G., Petrini, L., 2014. Fatigue behaviour of Nitinol peripheral stents: the role of plaque shape studied with computational structural analyses. Medical Engineering and Physics 36, 842–849. https://doi.org/.1037//0033-2909.I26.1.78

Gastaldi, D., Sassi, V., Petrini, L., Vedani, M., Trasatti, S., Migliavacca, F., 2011. Continuum damage model for bioresorbable magnesium alloy devices - Application to coronary stents. Journal of the Mechanical Behavior of Biomedical Materials 4, 352–365. https://doi.org/10.1016/j.jmbbm.2010.11.003

Gundert, T.J., Marsden, A.L., Yang, W., LaDisa, J.F., 2012. Optimization of Cardiovascular Stent Design Using Computational Fluid Dynamics. Journal of Biomechanical Engineering 134, 011002. https://doi.org/10.1115/1.4005542

Han, X., Wu, G., Li, Y., Li, M., 2006. A Novel Approach: Treatment of Bronchial Stump Fistula With a Plugged, Bullet-Shaped, Angled Stent. Annals of Thoracic Surgery 81, 1867–1871. https://doi.org/10.1016/j.athoracsur.2005.12.014

Irani, S., Kozarek, R., 2010. Esophageal stents: Past, present, and future. Techniques in Gastrointestinal Endoscopy 12, 178–190. https://doi.org/10.1016/j.tgie.2011.01.001

Isotalo, T.M., Nuutine, J.P., Vaajanen, A., Martikainen, P.M., Laurila, M., Törmälä, P., Talja, M., Tammela, T.L., 2006. Biocompatibility properties of a new braided biodegradable urethral stent: A comparison with a biodegradable spiral and a braided metallic stent in the rabbit urethra. BJU International 97, 856–859. https://doi.org/10.1111/j.1464-410X.2006.06000.x

Jedwab, M.R., Clerc, C.O., 1993. A study of the geometrical and mechanical properties of a self- expanding metallic stent—theory and experiment. Journal of applied biomaterials 4, 77–85.

Karanasiou, G.S., Papafaklis, M.I., Conway, C., Michalis, L.K., Tzafriri, R., Edelman, E.R., Fotiadis, D.I., 2017. Stents: biomechanics, biomaterials, and insights from computational modeling. Annals of Biomedical Engineering 45, 853–872. https://doi.org/10.1007/s10439-017-1806-8

Kim, J.H., Kang, T.J., Yu, W.R., 2008. Mechanical modeling of self-expandable stent fabricated using braiding technology. Journal of Biomechanics 41, 3202–3212. https://doi.org/10.1016/j.jbiomech.2008.08.005

Ma, D., Dargush, G.F., Natarajan, S.K., Levy, E.I., Siddiqui, A.H., Meng, H., 2012. Computer modeling of deployment and mechanical expansion of neurovascular flow diverter in patient-specific intracranial aneurysms. Journal of Biomechanics 45, 2256–2263. https://doi.org/10.1016/j.jbiomech.2012.06.013

McGee, O.M., Gunning, P.S., McNamara, A., McNamara, L.M., 2019. The impact of implantation depth of the LotusTM valve on mechanical stress in close proximity to the bundle of His. Biomechanics and Modeling in Mechanobiology 18, 79–88. https://doi.org/10.1007/s10237-018-1069-9

McHugh, P., Barakat, A., McGinty, S., 2016. Medical Stents: State of the Art and Future Directions. Annals of Biomedical Engineering 44, 274–275. https://doi.org/10.1007/s10439-015-1526-x

Midulla, M., Moreno, R., Baali, A., Chau, M., Negre-Salvayre, A., Nicoud, F., Pruvo, J.-P., Haulon, S., Rousseau, H., 2012. Haemodynamic imaging of thoracic stent-grafts by computational fluid dynamics (CFD): presentation of a patient-specific method combining magnetic resonance imaging and numerical simulations. European Radiology 22, 2094–2102. https://doi.org/10.1007/s00330-012-2465-7

Morlacchi, S., Migliavacca, F., 2013. Modeling stented coronary arteries: where we are, where to go. Annals of Biomedical Engineering 41, 1428–1444. https://doi.org/10.1007/s10439-012-0681-6

Peirlinck, M., Debusschere, N., Iannaccone, F., Siersema, P.D., Verhegghe, B., Segers, P., De Beule, M., 2018. An in silico biomechanical analysis of the stent–esophagus interaction. Biomechanics and Modeling in Mechanobiology 17, 111–131. https://doi.org/10.1007/s10237-017-0948-9

Petrini, L., Trotta, A., Dordoni, E., Migliavacca, F., Dubini, G., Lawford, P. V., Gosai, J.N., Ryan, D.M., Testi, D., Pennati, G., 2016. A Computational Approach for the Prediction of Fatigue Behaviour in Peripheral Stents: Application to a Clinical Case. Annals of Biomedical Engineering 44, 536–547. https://doi.org/10.1007/s10439-015-1472-7

Raju, S., 2013. Best management options for chronic iliac vein stenosis and occlusion. Journal of Vascular Surgery 57, 1163–1169. https://doi.org/10.1016/j.jvs.2012.11.084

Ronchey, S., Praquin, B., Orrico, M., Serrao, E., Ciceroni, C., Alberti, V., Fazzini, S., Mangialardi, N., 2016. Outcomes of 1000 carotid Wallstent implantations: single-center experience. Journal of Endovascular Therapy 23, 267–274. https://doi.org/10.1177/1526602815626558

Seigerman, M.E., Nathan, A., Anwaruddin, S., 2019. The Lotus valve system: an in-depth review of the technology. Current Cardiology Reports 21, 157. https://doi.org/10.1007/s11886-019-1234-5

Shanahan, C., Tiernan, P., Tofail, S.A.M., 2017a. Looped ends versus open ends braided stent: A comparison of the mechanical behaviour using analytical and numerical methods. Journal of the Mechanical Behavior of Biomedical Materials 75, 581–591. https://doi.org/10.1016/j.jmbbm.2017.08.025

Shanahan, C., Tofail, S.A.M., Tiernan, P., 2017b. Viscoelastic braided stent: Finite element modelling and validation of crimping behaviour. Materials and Design 121, 143–153. https://doi.org/10.1016/j.matdes.2017.02.044

Sturla, F., Ronzoni, M., Vitali, M., Dimasi, A., Vismara, R., Preston-Maher, G., Burriesci, G., Votta, E., Redaelli, A., 2016. Impact of different aortic valve calcification patterns on the outcome of transcatheter aortic valve implantation: A finite element study. Journal of Biomechanics 49, 2520–2530. https://doi.org/10.1016/j.jbiomech.2016.03.036

Verhegghe, B., 2013. pyFormex Documentation.

Wang, R., Ravi-Chandar, K., 2004a. Mechanical Response of a Metallic Aortic Stent—Part I: Pressure-Diameter Relationship. Journal of Applied Mechanics 71, 697–705. https://doi.org/10.1115/1.1782650

Wang, R., Ravi-Chandar, K., 2004b. Mechanical Response of a Metallic Aortic Stent—Part II: A Beam-on-Elastic Foundation Model. Journal of Applied Mechanics 71, 706–712. https://doi.org/10.1115/1.1782912

Záhora, J., Bezrouk, A., Hanuš, J., 2007. Models of stents - Comparison and applications. Physiological Research 56, 115–121.

Zhao, F., Xue, W., Wang, F., Sun, J., Lin, J., Liu, L., Sun, K., Wang, L., 2019. Braided bioresorbable cardiovascular stents mechanically reinforced by axial runners. Journal of the Mechanical Behavior of Biomedical Materials 89, 19–32. https://doi.org/10.1016/j.jmbbm.2018.09.003

Zhao, S., Liu, X. (Cheryl), Gu, L., 2012. The Impact of Wire Stent Fabrication Technique on the Performance of Stent Placement. Journal of Medical Devices 6, 011007. https://doi.org/10.1115/1.4005788

Figure legends

Fig. 1. Braided stents characterized by open or looped ends and cylindrical or variable section geometries on the longitudinal (ZY) and transversal (XY) planes (left). The geometrical parameters used in the 3D parametric equations are shown on the Wallstent views (top-left corner, top-center). Wallstent with the global coordinate system (XYZ) and a magnification of the mesh with a connector element, joining the nodes marked with the green triangle and square, and the relative local axis (rϑz) (right).

Fig. 2. Schemes of the performed simulations. a) Bending: the extremities of the undeformed stent (green) were connected through MPC to two reference nodes, RP1 and RP2. Referring to the global reference system, a rotation around the X-axis was applied to RP1 and RP2, while all other degrees of freedom were locked apart for the Z translation of RP2. In blue the final configuration. Z_{disp} = Z translation of RP2, Y_{disp} = Y translation in the middle section. b) Crimping: 12 planes were radially moved (right) in order to reduce the stent diameter (left). ΔL = length variation between the stent undeformed (green) and final (blue) configurations, ΔD_{middle} and ΔD_{side} = diameter reduction in the middle and side sections. c) Confined release: the crimped stent (green) was self-expanded in an idealized stenotic rigid vessel. H_p = maximum thickness of the concentric plaque, D_V = healthy vessel inner diameter.

Fig. 3. Bending test: deformed configurations with Von Mises stress colored map.

Fig. 4. Bending test: comparison among the GC, H and J models concerning reaction moment, linear displacement of RP2 in the Z direction and linear displacement of the central section in the Y direction with respect to the rotational displacement applied in RP2 and RP1.

Fig. 5. Crimping test: deformed configurations with Von Mises stress colored map. D_{ext} and D_{int} are the final diameters of the external and internal side nodes of the Wallstent respectively

Fig. 6 Crimping test: comparison among the GC, H and J models concerning crimping force, diameter variation (in the middle and in the side sections) and length variation.

Fig. 7. Confined release: deformed configurations with Von Mises stress colored map (left) and contact pressure distributions on the rigid vessel (right). The maximum contact pressure values are reached only in localized spot within the dotted red rectangles.

Fig. 8. Confined release: force acting on the rigid vessel, evaluated both in the middle (blue bar), in the lateral portions (yellow bar) of the vessel and as a sum of all the contributions (red bar).

Figure 1

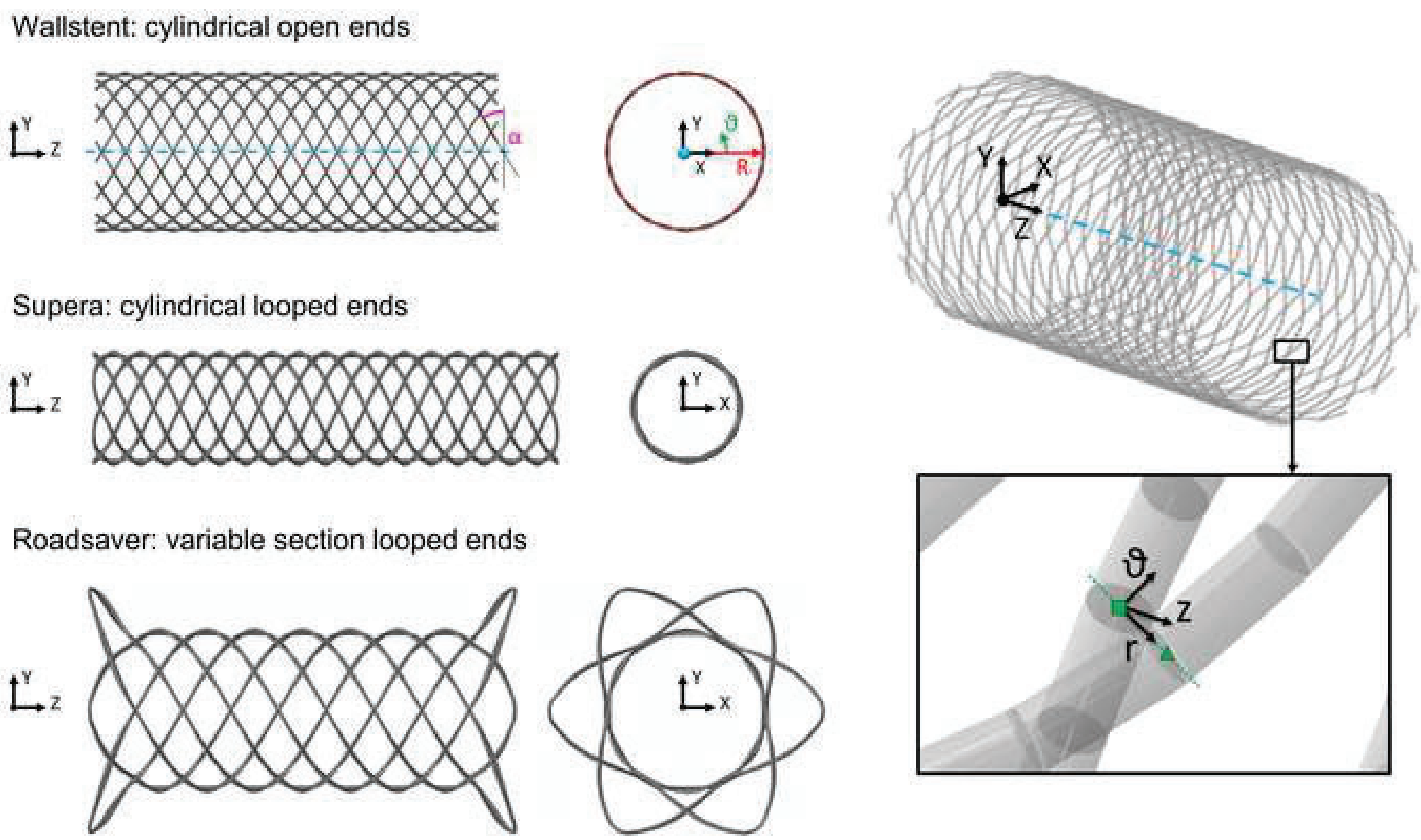
Wallstent: cylindrical open ends
Supera: cylindrical looped ends
Roadsaver: variable section looped ends
Y
Z
X
R
ϑ
α
r

Figure 2

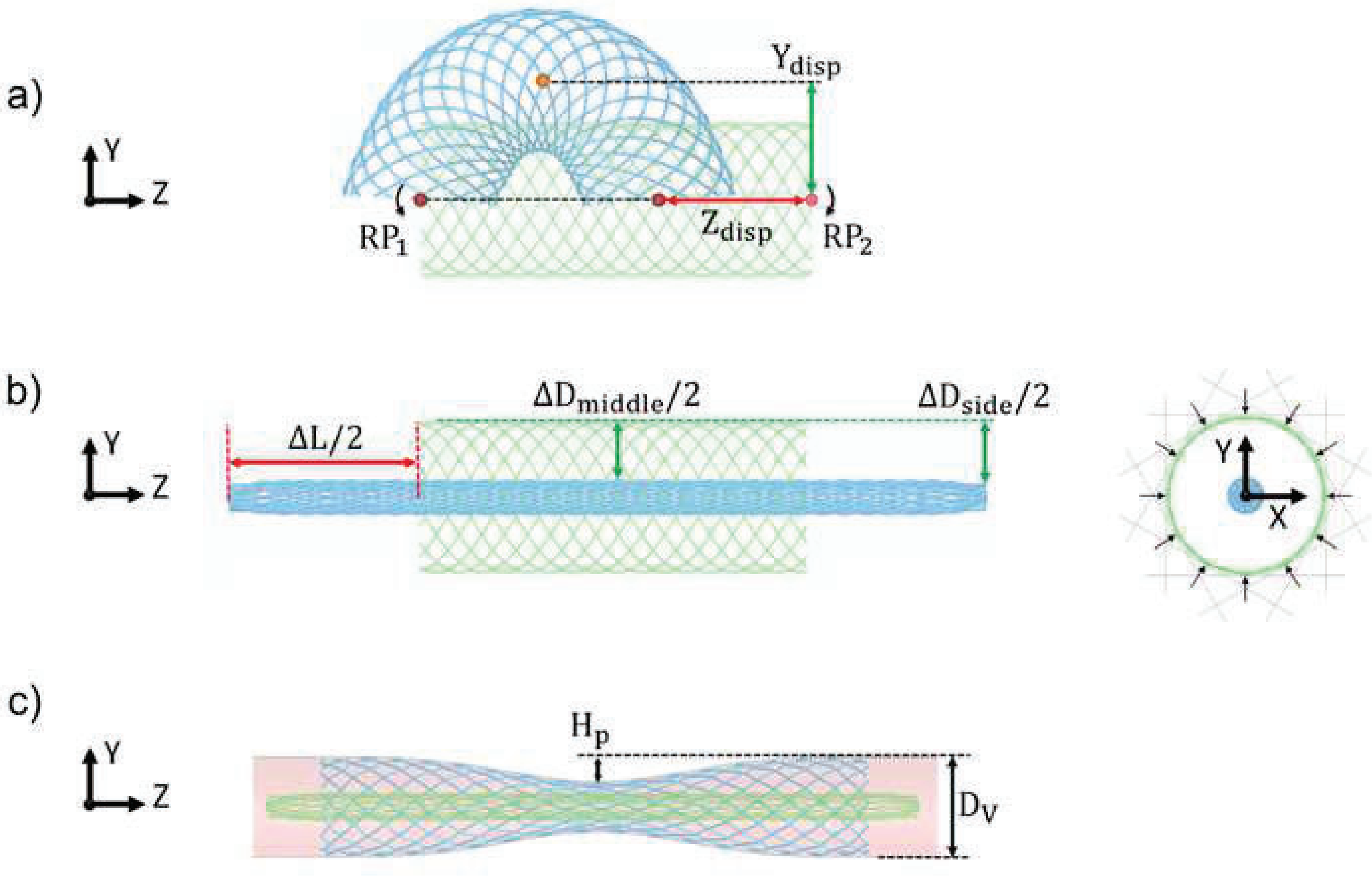
a)
Y
Z
Y_disp
Z_disp
RP_1
RP_2
b)
Y
Z
ΔL/2
ΔD_middle/2
ΔD_side/2
Y
X
c)
Y
Z
H_p
D_V

Figure 3

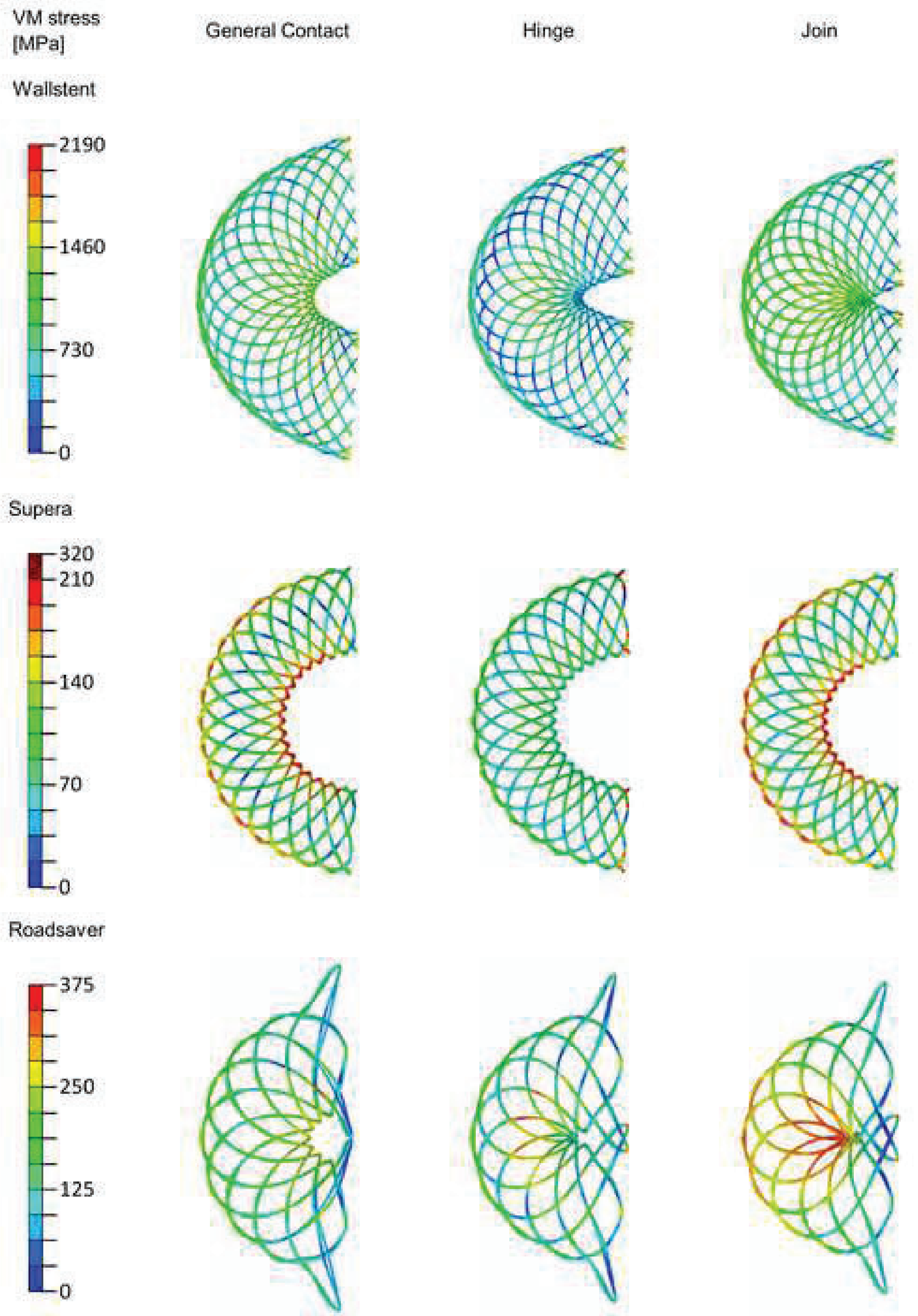

VM stress [MPa]
General Contact
Hinge
Join
Wallstent
2190
1460
730
0
Supera
320
210
140
70
0
Roadsaver
375
250
125
0

Figure 4

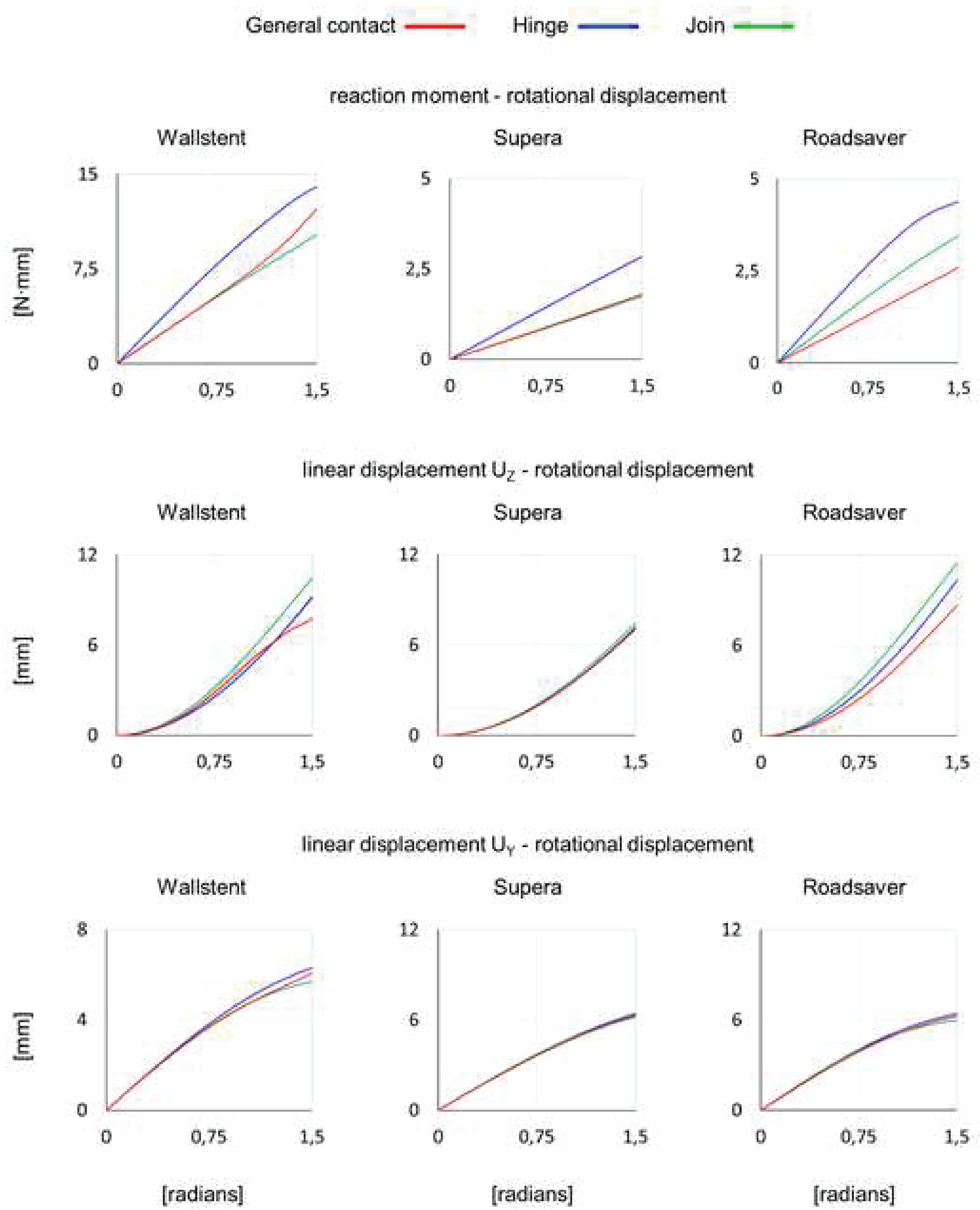

General contact
Hinge
Join
reaction moment - rotational displacement
Wallstent
Supera
Roadsaver
[N·mm]
15
7,5
0
5
2,5
0
0,75
1,5
linear displacement U_Z - rotational displacement
[mm]
12
6
linear displacement U_Y - rotational displacement
8
4
[radians]

Figure 5

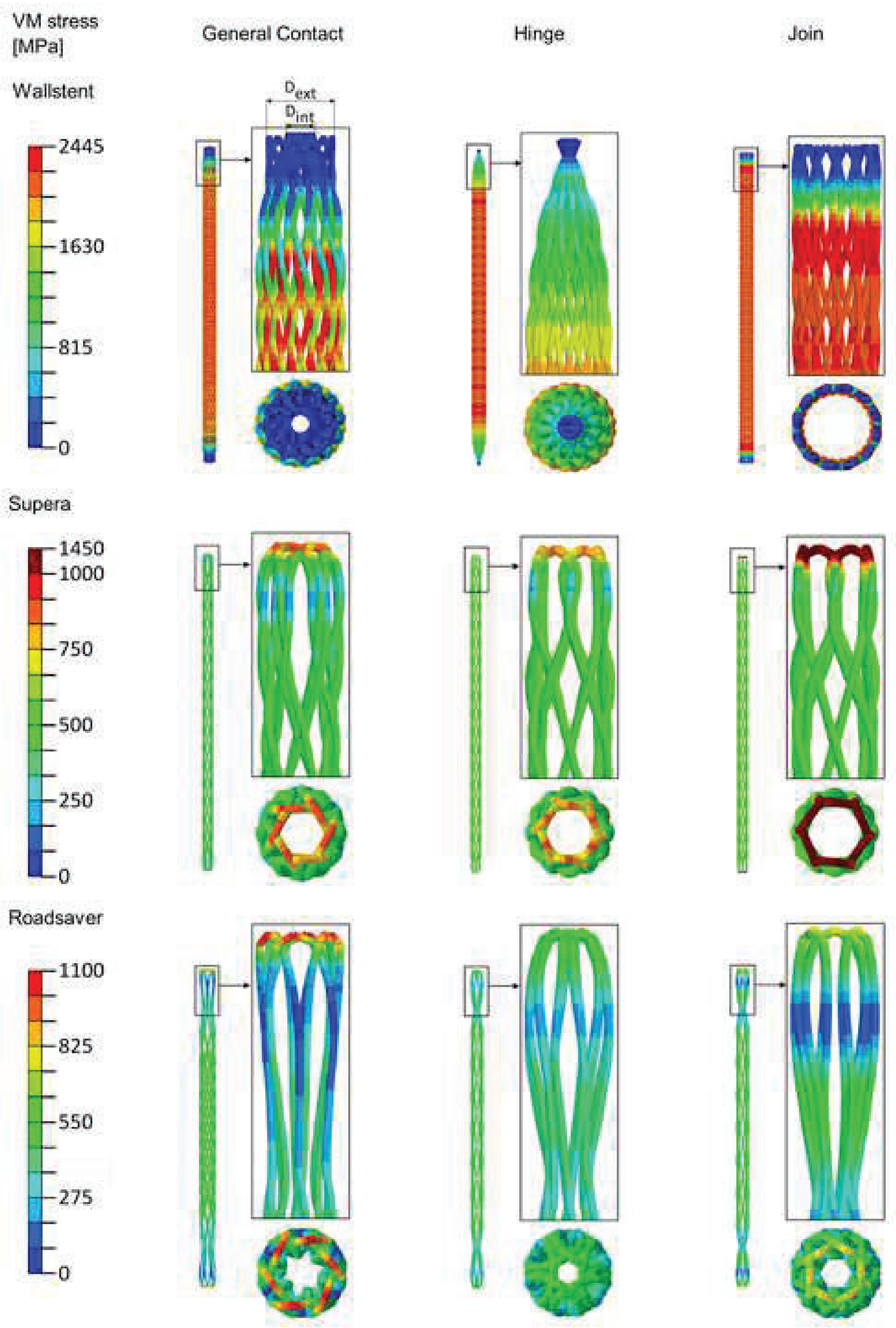

VM stress [MPa]
General Contact
Hinge
Join
Wallstent
D_{ext}
D_{int}
2445
1630
815
0
Supera
1450
1000
750
500
250
0
Roadsaver
1100
825
550
275
0

Figure 6

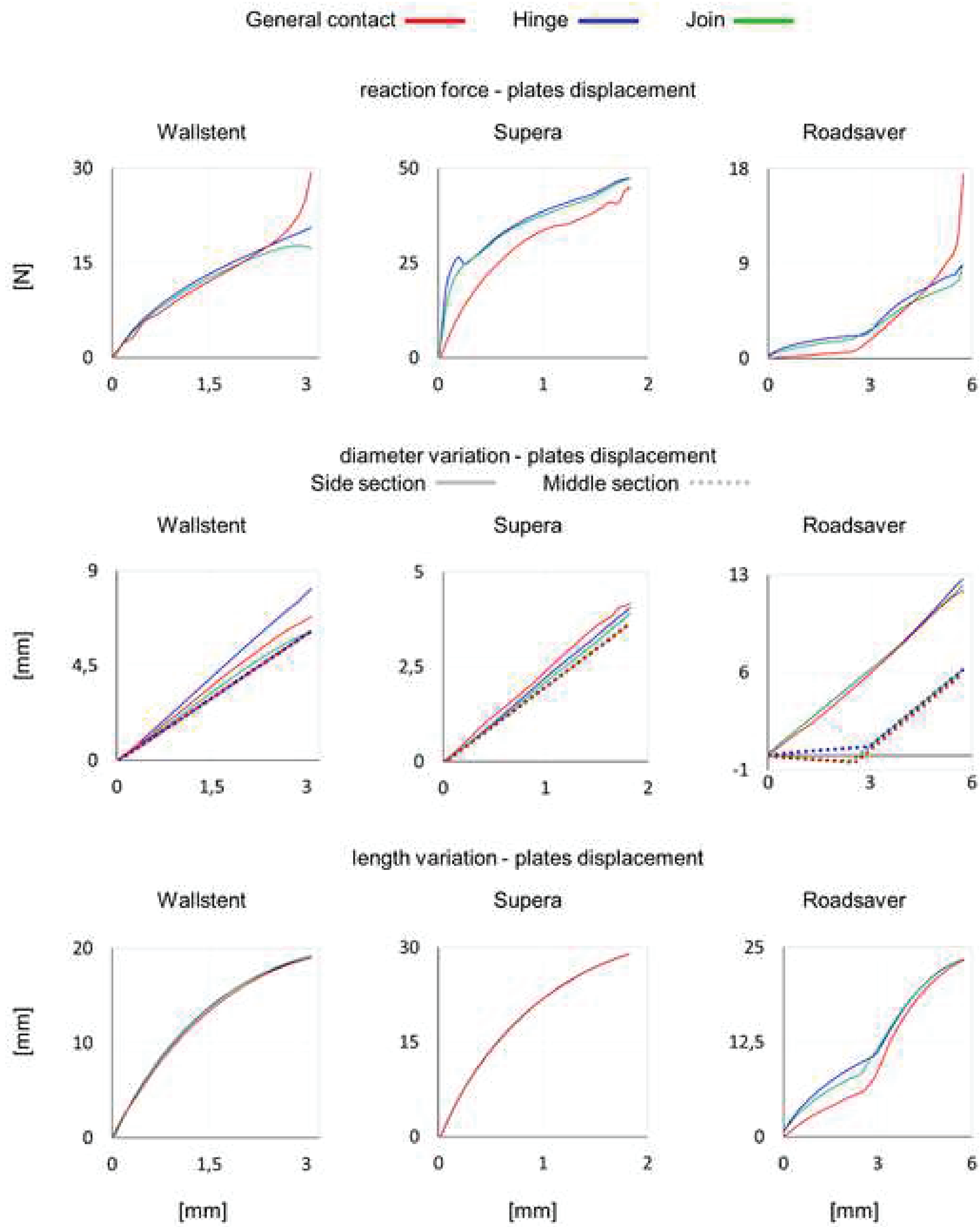

General contact
Hinge
Join
reaction force - plates displacement
Wallstent
Supera
Roadsaver
[N]
30
15
0
0
1,5
3
50
25
0
0
1
2
18
9
0
0
3
6
diameter variation - plates displacement
Side section
Middle section
Wallstent
Supera
Roadsaver
[mm]
9
4,5
0
0
1,5
3
5
2,5
0
0
1
2
13
6
-1
0
3
6
length variation - plates displacement
Wallstent
Supera
Roadsaver
[mm]
20
10
0
0
1,5
3
30
15
0
0
1
2
25
12,5
0
0
3
6
[mm]
[mm]
[mm]

Figure 7

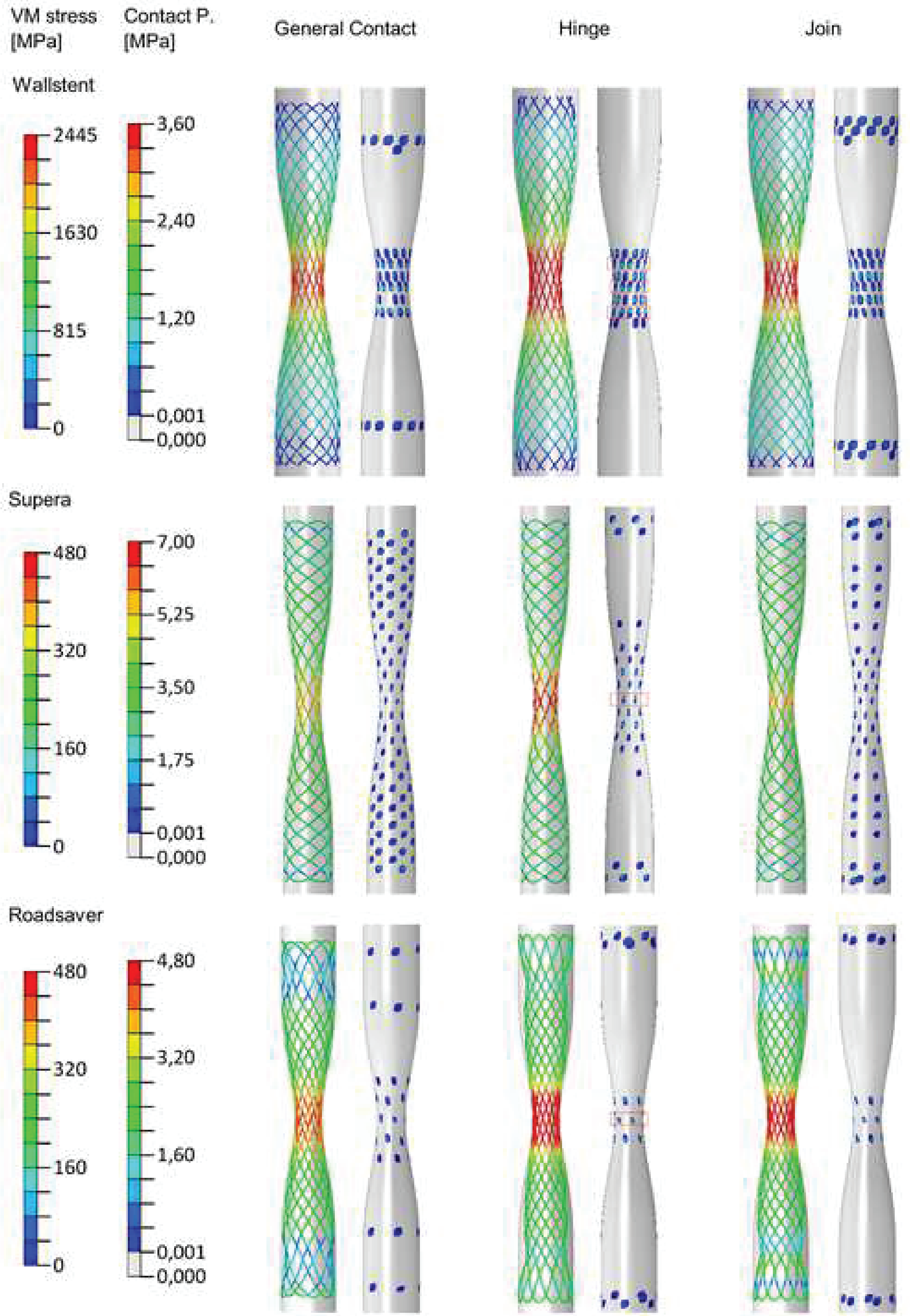

VM stress [MPa]
Contact P. [MPa]
General Contact
Hinge
Join
Wallstent
2445
1630
815
0
3,60
2,40
1,20
0,001
0,000
Supera
480
320
160
0
7,00
5,25
3,50
1,75
0,001
0,000
Roadsaver
480
320
160
0
4,80
3,20
1,60
0,001
0,000

Figure 8

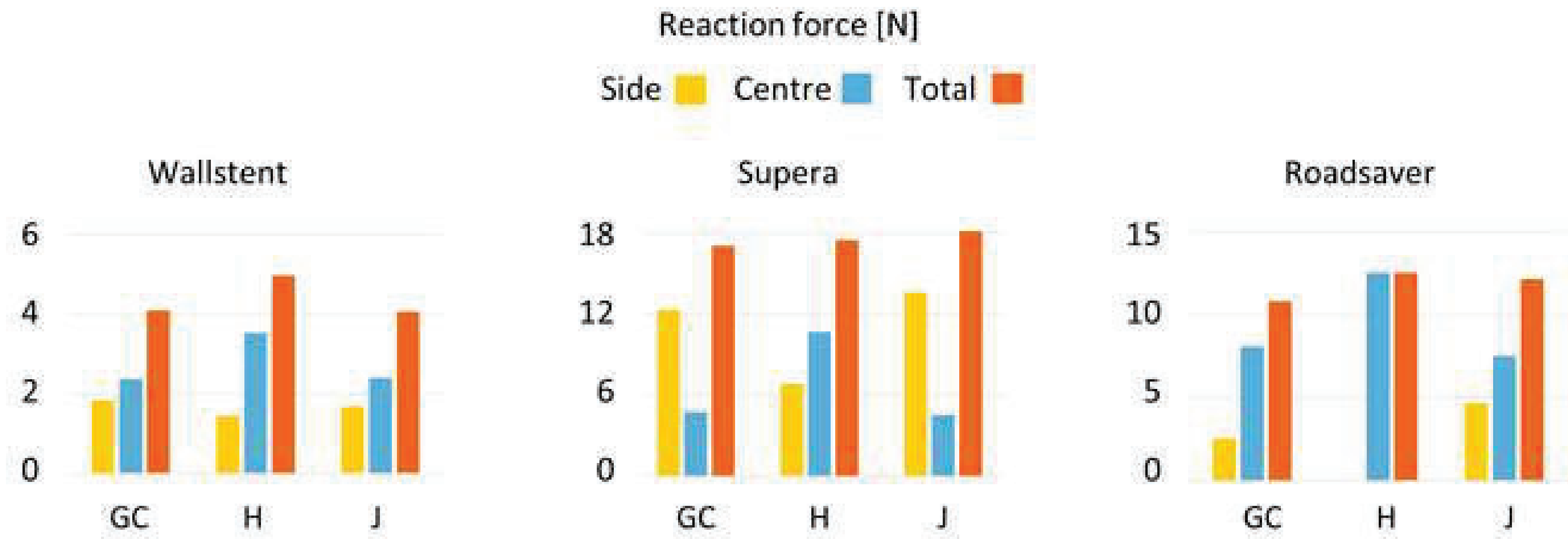

Reaction force [N]
Side
Centre
Total
Wallstent
Supera
Roadsaver
6
4
2
0
18
12
6
0
15
10
5
0
GC
H
J
GC
H
J
GC
H
J

Tables

Table 1. Geometrical parameters for the stent reconstruction and number of elements for the model discretization (N_{el}) (top): wire radius (r), external stent radius (R_{ext}), stent length (L), pitch angle (α) and the number of wires in the clockwise direction (n). Geometrical parameters of the stenotic rigid vessel (Fig. 3c) for the confined release simulation (bottom): healthy vessel inner diameter (D_V), maximum thickness of the concentric plaque (H_p), residual stenosis ($RS = (D_V - 2H_p)/D_V$), plaque length (L_P) and sharpness of the peak (s).

Stents	r [mm]	R_{ext} [mm]	L [mm]	α [°]	n	N_{el}
Wallstent	0.065	4	20	30	12	3264
Supera	0.09 (Myint et al., 2016)	2.75	22	25	6	1728
Roadsaver	0.09 (Wissgott et al., 2015)	4	20.5	30	6	960
Vessels	D_V [mm]	H_p [mm]	RS [-]	L_P [mm]	s [-]	
Wallstent	6	1.5	0.5	40	5	
Supera	5	1.25	0.5	40	5	
Roadsaver	6	1.5	0.5	40	5	

Table 2. Percent difference of the Hinge (H) and Join (J) model with respect to the general contact option, in terms of: reaction moments/forces (RM, RF, RF_{center}, RF_{side}, RF_{total}), maximum Von Mises stress (Max. σ_{VM}), linear displacements (U_Z, U_Y) and deformations magnitude (ΔD_{side}, ΔL).

Percent difference [%]	**Wallstent**		**Supera**		**Roadsaver**	
	H	**J**	**H**	**J**	**H**	**J**
Bending						
RM	14,33	-16,57	57,95	-3,13	69,41	34,02
Max. σ_{VM}	0,32	-1,30	57,66	0,51	3,78	6,17
U_Z	17,49	34,61	1,29	5,25	19,36	32,80
U_Y	3,71	-6,17	3,08	1,40	2,72	-4,60
Crimping						
RF	-29,93	-41,09	6,35	6,17	-49,44	-50,39
Max. σ_{VM}	-7,03	0,00	-7,78	60,44	-48,27	-28,17
ΔD_{side}	19,44	-10,45	-2,63	-6,14	6,80	3,01
ΔL	-0,15	1,05	0,15	0,15	0,30	0,23
Confined release						
RF_{center}	55,64	-7,21	126,04	-4,39	49,05	1,37
RF_{side}	-100,00	84,73	-44,76	10,46	-20,71	-8,29
RF_{total}	15,91	12,22	2,56	6,35	21,28	-0,70
Max. σ_{VM}	4,69	2,19	20,02	19,53	0,22	-2,67

Appendices

A. Mesh sensitivity

The mesh sensitivity was carried out on a single helical wire with length equal to 10mm. The same geometrical parameters adopted to replicate the Wallstent device were used. The lower extremity was fixed while the upper one was moved to stretch the helix of 10mm.

Both structured hexahedral meshes (C3D8I) and beam meshes (B31) were analyzed to ensure the convergence of the results (Table A.1). While the results obtained with the 3D meshes highlight a significant influence of the mesh refinement, no relevant differences were visible among the beam meshes considered.

Therefore, the differences between beam elements and 3D elements were assessed in terms of reaction force and maximum von Mises stress (Table A.2). Since the deviations from the finest hexahedral model are lower than 2.1% and 6.5% on the maximum reaction force and von Mises stress respectively, beam elements were considered suitable for the present work.

For the beam meshes, also contact thickness reductions were identified (Table A.2). Indeed, if the beam length is lower than a certain fraction of the beam section size, the contact thickness is reduced to avoid spurious self-contact, without affecting stiffness calculation. The coarsest beam mesh ensures the correct contact beam thickness is maintained (0.13mm) slightly increasing the error on the maximum von Mises stress. Instead, both the finest and the middle beam meshes feature a reduced contact section diameter (equal to 0.059mm and 0.117mm respectively).

Thus, all the meshes of the illustrated braided stents were generated using beams short enough to describe the wire curvature and long enough to prevent thickness reduction.

Table A.1. Beam section with three hexahedral meshes (left) and trait of a wire corresponding to $\vartheta \in \left[0, \frac{\pi}{n}\right]$ meshed with three different beam length (right). The approximate dimensions (size) and the total number of the elements (N_{el}) are reported.

	MESH 3D (C3D8I)		MESH BEAM (B31)	
	Mesh1	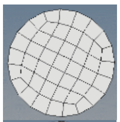	**Mesh1B**	
size [mm]	0.02		0.1	
N_{el}	63720		288	
	Mesh2	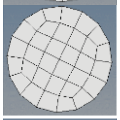	**Mesh2B**	
size [mm]	0.025		0.2	
N_{el}	36096		144	
	Mesh3	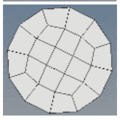	**Mesh3B**	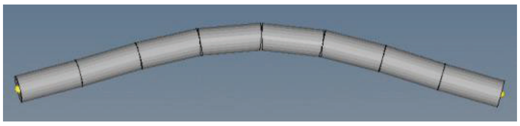
size [mm]	0.035		0.3	
N_{el}	16884		96	

Table A.2. On the left, the percent differences with respect to the finest 3D mesh (Mesh1) in terms of maximum force (F_{max}) and maximum von Mises stress (Max. σ_{VM}) are shown. On the right, the force-displacement plots for the different meshes are compared.

Percent diffence [%]	F_{max}	Max. σ_{VM}
C3D8I		
Mesh1	-	-
Mesh2	2.08	0.39
Mesh3	6.88	1.39
B31		
Mesh1B	2.04	5.78
Mesh2B	1.80	6.03
Mesh3B	2.02	6.23

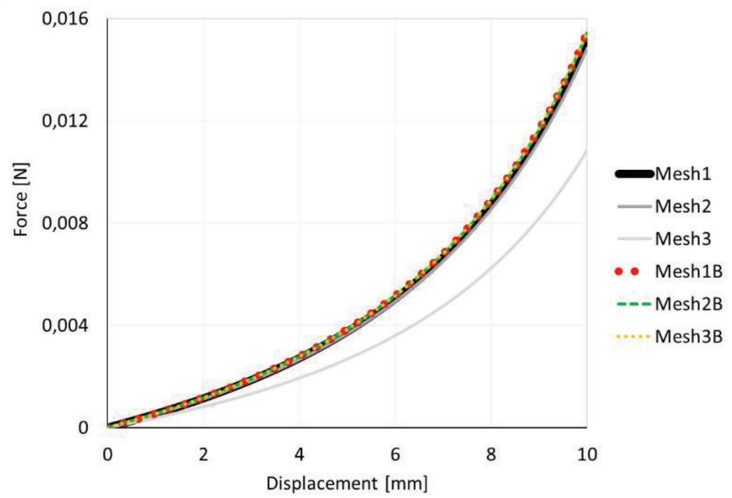

B. Material models and parameters

The Wallstent is made of Phynox, a cobalt-chromium alloy: for describing its mechanical behavior an elastic-plastic model with isotropic hardening was adopted. The material parameters were taken from the literature (De Beule et al., 2009; Auricchio et al., 2011) and their values are reported in Table B.1.

The Supera and Roadsaver stents are made of Nitinol, a nickel-titanium alloy. Above a specific temperature value (Af), Nitinol has a super-elastic behavior (Fig. B.1), due to the coexistence of two solid phases (austenite and martensite): it allows Ni-Ti structures to elastically recover their original shape even after large deformations are applied. For describing the mechanical behavior of Nitinol, the constitutive model available in Abaqus for super-elastic material was adopted. The material parameters were taken from the literature (Conti, 2007) and their values are reported in Table B.2.

Table B.1. Phynox material parameters: elastic modulus (E), yield strength (σ_{yield}), Poisson's ratio (ν), density (ρ).

Phynox material parameters			
E [MPa]	σ_{yield} [MPa]	ν [-]	ρ [g/cm3]
260000	2450	0.33	8

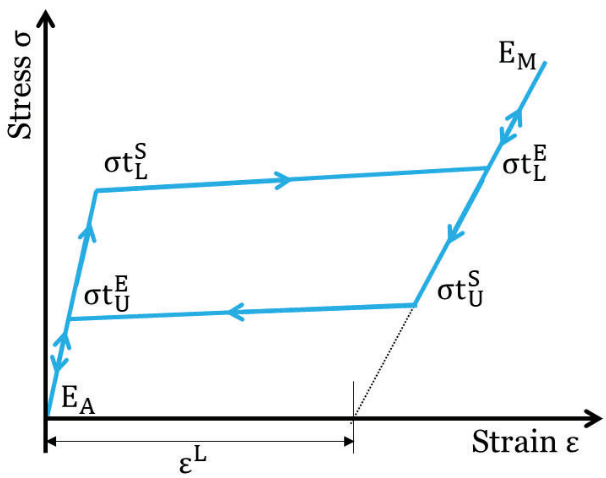

Fig. B.1. Nitinol pseudo-elastic behavior: EA and EM are respectively the elastic moduli of the austenitic and martensitic phases; the stress values reported in the figure indicate the start/end-point of the load/unload transformation plateau in tension ($\sigma t_{L/U}^{S/E}$); ε^L is the strain value near the intersection between the martensitic branch and the strain axis.

Table B.2. Nitinol material parameters: austenite elastic modulus (E_A), martensite elastic modulus (E_M), start/end of transformation phase during loading/unloading (σt_L^S, σt_L^E, σt_U^S, σt_U^E), Poisson's ratio (ν), transformation strain (ε_L), reference temperature (T_0), beta parameter ($\partial\sigma t/\partial T$) and density ($\rho$). See also Figure B.1 for the meaning of the parameters.

Nitinol material parameters										
E_A [MPa]	E_M [MPa]	σt_L^S [MPa]	σt_L^E [MPa]	σt_U^S [MPa]	σt_U^E [MPa]	ν [-]	ε_L [-]	T_0 [°C]	$\partial\sigma/\partial T$ [MPa/°C]	ρ [g/cm^3]
35877	24462	489	572	230	147	0.33	0.0555	22	6.7	6.7

C. Model validation

In the paper, the general contact was assumed as the most accurate contact model methodology. In order to verify this assumption, we referred to the work of Kim et al. (Kim et al., 2008) where experimental tests on braided stents in a complex configuration were performed: six cylindrical open ends stents (similar to the Wallstent) were compressed to half their original diameters between a plane and a circular rod with a diameter of 10mm (Fig. C.1a). This type of load condition is particularly interesting because it involves not axisymmetric deformations that allow to highlight differences between the three contact strategies: general contact algorithm, Hinge connectors, Join connectors. In particular, the A45 sample was reconstructed and the experimental test numerically replicated using the three different strategies. Abaqus explicit solver was used. The kinetic energy and the viscous dissipation were kept lower than the 5% of the internal energy throughout most of the process.

In Fig. C.1b the computational results are compared with the experimental curve and the numerical prediction obtained by Kim et al. (Kim et al., 2008), also using the Abaqus general contact algorithm.

While the models exploiting the general contact algorithm show a good agreement with the experimental data, substantial differences both concerning load values and hysteretic behavior are visible when the connector models are considered.

a)

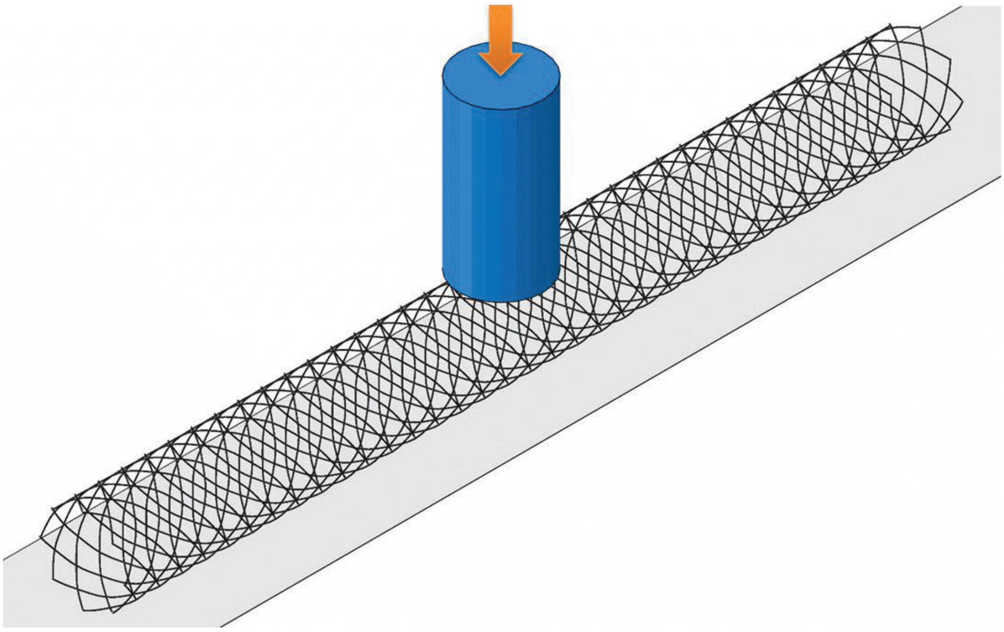

b)

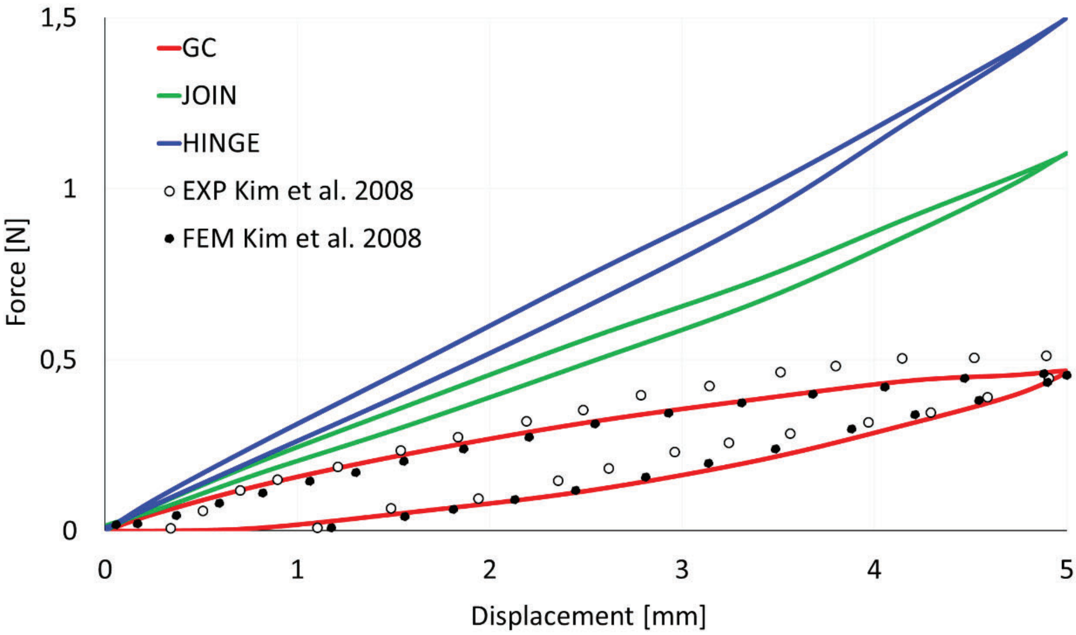

Fig. C.1. a) illustration of the compression test performed by Kim et al. (Kim et al., 2008). b) force-displacement plots obtained with the GC (general contact algorithm), H (Hinge connectors) and J (Join connectors) models compared with the experimental (EXP) and numerical (FEM) curves from the article of Kim et al. (Kim et al., 2008).

D. Impact of local curvature

The geometry reconstruction of braided stents is complicated by the woven structure. However, this feature should not be neglected. Indeed, in some configurations, the local wire curvature may introduce kinematic restrictions, constraining the relative slip among the wires.

Note that, increasing the wires' diameter, all else being equal, the distance of the overlapping points increases and thus also the local wire curvature, reinforcing its impact. To better explicate this aspect, the Wallstent bending test was replicated (Fig. D.1), varying the wire diameter (from 0.13mm to 0.23mm).

The results obtained with the general contact and with the simplified models involving connector elements were compared in terms of deformed configuration (Fig. D.2), reaction moment, and linear displacements (Fig. D.3). The kinematic effects of the increased overall dimensions are observable only when the general contact is applied since, in the simplified models, the interaction among the wires was neglected. In the former option, this enhanced constraint restricts the displacement along the Z-axis (Fig. D.3 middle), leading to a different deformed configuration (Fig. D.2) and consequently to an intensified stiffening with respect to the one recorded in the simplified models (Fig. D.3 left). Similar conclusions can be extrapolated observing the percent differences of the models based on the hinge (H) and join (J) connectors with respect to the general contact option that are reported in Table D.1.

Finally, the intertwining is a critical feature of braided stents that should not be neglected in the modeling process. Indeed, the interaction among the wires may introduce kinematic constraints, whose impact depends on the geometrical parameters and is not observable in the simplified models.

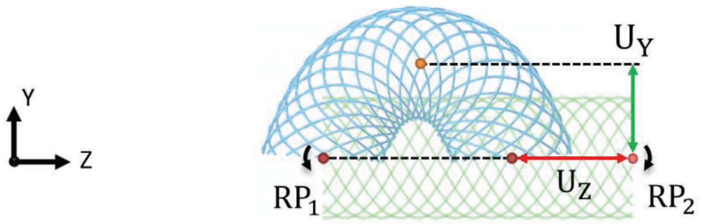

Fig. D.1. Bending test: the extremities of the undeformed stent (green) were connected to two reference nodes, RP1 and RP2. Referring to the global reference system, a rotation around the X-axis was applied to RP1 and RP2, while all other degrees of freedom were locked apart for the Z translation of RP2. In blue the final configuration. U_Z = Z translation of RP2, U_Y = Y translation in the middle section.

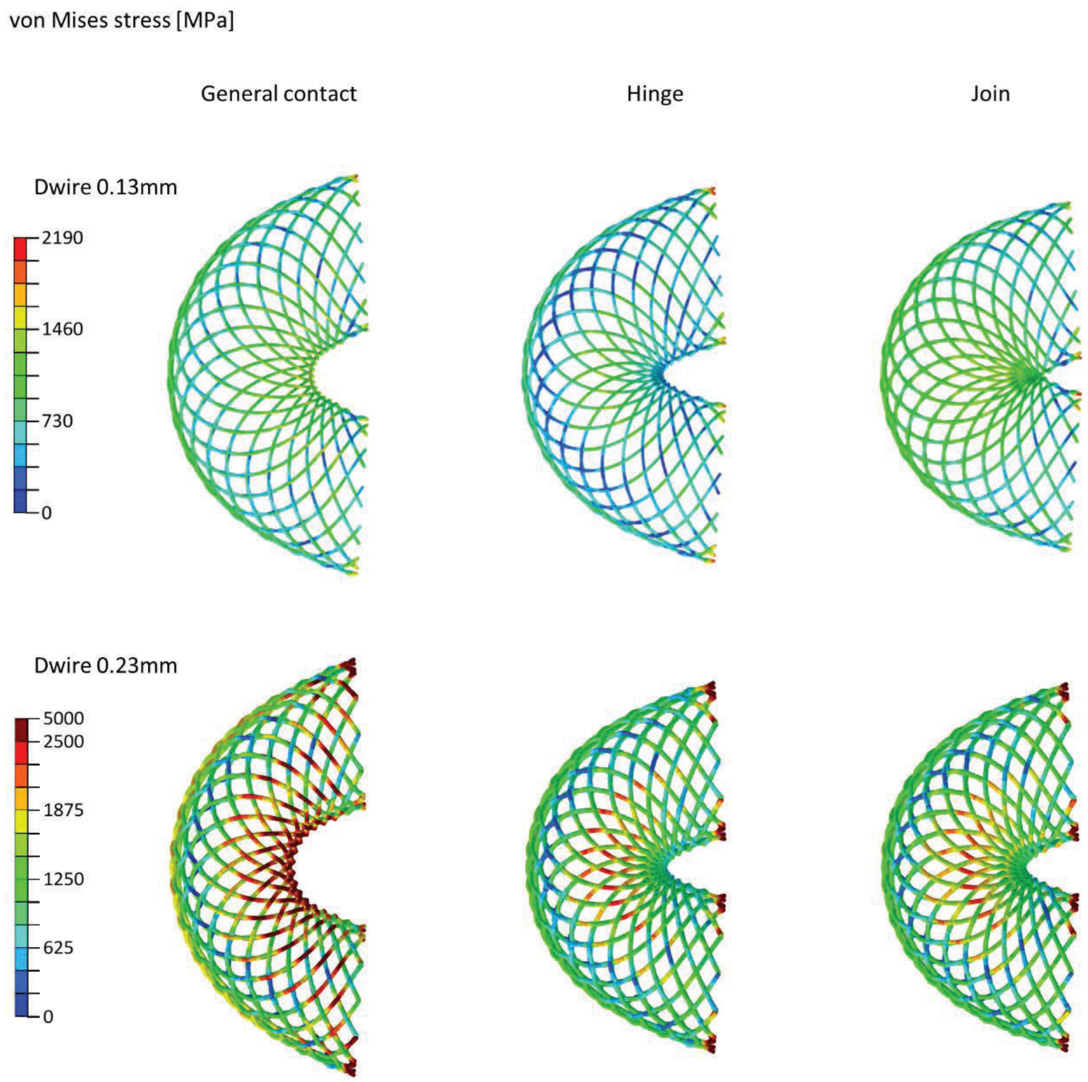

Fig. D.2. Bending test: deformed configurations with Von Mises stress colored map.

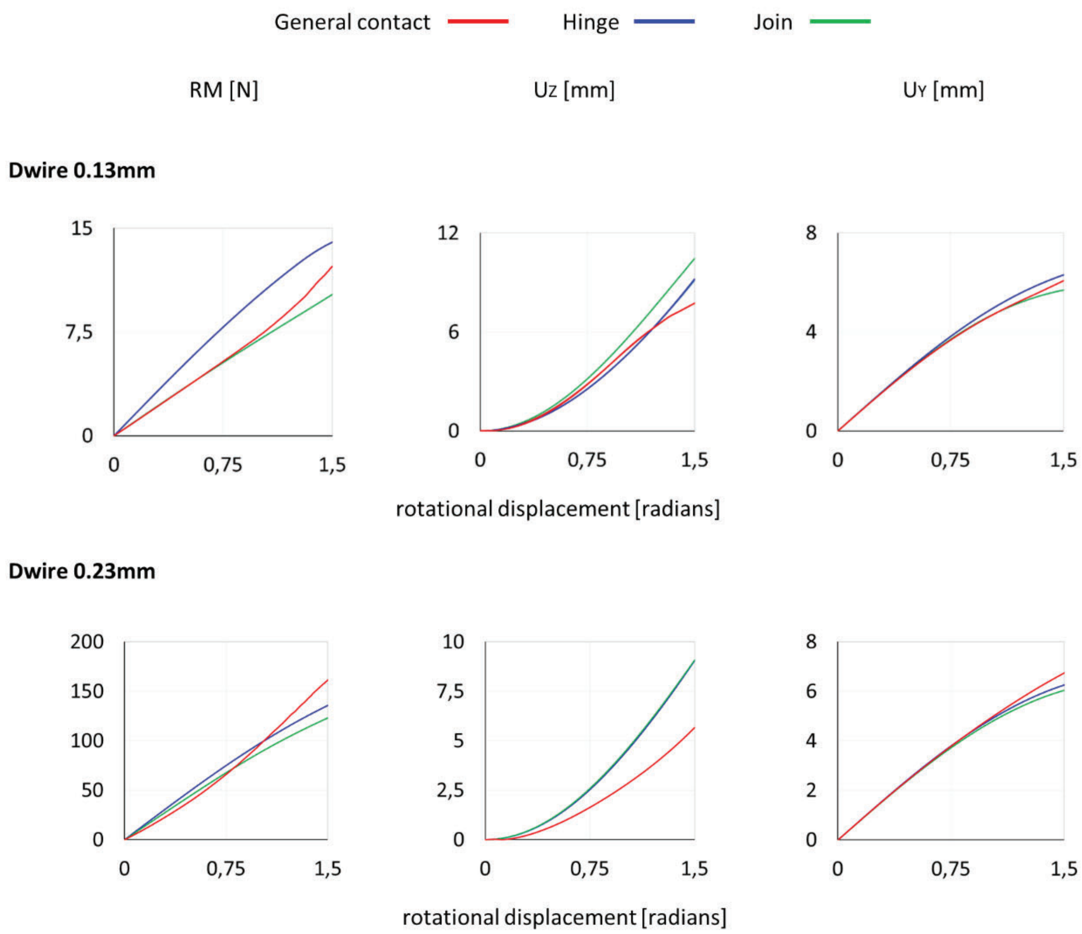

Fig. D.3. Bending test: comparison among the GC, H and J models concerning reaction moment, linear displacement of RP2 in the Z direction and linear displacement of the central section in the Y direction with respect to the rotational displacement applied in RP2 and RP1.

Table D.1. Percent difference of the Hinge (H) and Join (J) model with respect to the general contact option, in terms of reaction moments (RM) and linear displacements (UZ, UY).

	Dwire 0.23mm		**Dwire 0.13mm**	
diff%	**H**	**J**	**H**	**J**
RM	14,33	-16,57	-15,77	-23,79
UZ	17,49	34,61	59,67	60,29
UY	3,71	-6,17	-7,21	-10,45

References

Auricchio, F., Conti, M., De Beule, M., De Santis, G., Verhegghe, B., 2011. Carotid artery stenting simulation: From patient-specific images to finite element analysis. Medical Engineering and Physics 33, 281–289. https://doi.org/10.1016/j.medengphy.2010.10.011

Conti, M., 2007. Finite Element Analysis of self-expanding braided wirestent (MSc Thesis, Ghent University).

De Beule, M., Van Cauter, S., Mortier, P., Van Loo, D., Van Impe, R., Verdonck, P., Verhegghe, B., 2009. Virtual optimization of self-expandable braided wire stents. Medical Engineering and Physics 31, 448–453. https://doi.org/10.1016/j.medengphy.2008.11.008

Kim, J.H., Kang, T.J., Yu, W.R., 2008. Mechanical modeling of self-expandable stent fabricated using braiding technology. Journal of Biomechanics 41, 3202–3212. https://doi.org/10.1016/j.jbiomech.2008.08.005